Additively manufactured bioceramic scaffolds based on triply periodic minimal surfaces for bone regeneration

Hong Zhu[1]***ID**, **Jinsi Wang**[1]*, **Shengfa Wang**[2], **Yue Yang**[1],
Meiyi Chen[1], **Qifei Luan**[1], **Xiaochuan Liu**[1], **Ziheng Lin**[1], **Jiaqi Hu**[1],
**Kenny Man**[3,4] **and Jingying Zhang**[1]

Abstract

The study focused on the effects of a triply periodic minimal surface (TPMS) scaffolds, varying in porosity, on the repair of mandibular defects in New Zealand white rabbits. Four TPMS configurations (40%, 50%, 60%, and 70% porosity) were fabricated with β-tricalcium phosphate bioceramic via additive manufacturing. Scaffold properties were assessed through scanning electron microscopy and mechanical testing. For proliferation and adhesion assays, mouse bone marrow stem cells (BMSCs) were cultured on these scaffolds. In vivo, the scaffolds were implanted into rabbit mandibular defects for 2 months. Histological staining evaluated osteogenic potential. Moreover, RNA-sequencing analysis and RT-qPCR revealed the significant involvement of angiogenesis-related factors and Hippo signaling pathway in influencing BMSCs behavior. Notably, the 70% porosity TPMS scaffold exhibited optimal compressive strength, superior cell proliferation, adhesion, and significantly enhanced osteogenesis and angiogenesis. These findings underscore the substantial potential of 70% porosity TPMS scaffolds in effectively promoting bone regeneration within mandibular defects.

Keywords

Graphical abstract
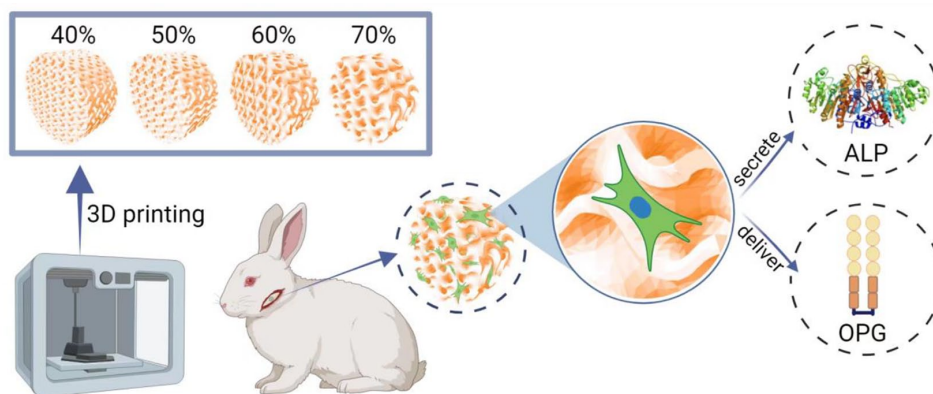
[1]The First Dongguan Affiliated Hospital, Guangdong Medical University, Dongguan, P.R. China
[2]Dalian University of Technology, Dalian, P.R. China
[3]Department of Oral and Maxillofacial Surgery & Special Dental Care University Medical Center Utrecht, Utrecht, The Netherlands
[4]Regenerative Medicine Center Urecht, Utrecht, The Netherlands

*These authors are co-first authors.

Corresponding author:
Jingying Zhang, The First Dongguan Affiliated Hospital, Guangdong Medical University, No. 42 Jiaoping Avenue, Tangxia Town, Dongguan 523710, P.R. China.
Email: zhangjy@gdmu.edu.cn

Introduction

The maxillofacial regions, including the maxilla and nasal bones, serve as crucial supporting structures for maintaining facial contours and performing functions such as speech and mastication.[1] Bone defects in the maxillofacial region caused by tumor resection, trauma, and osteonecrosis[2] (radiogenic osteonecrosis and drug-related osteonecrosis) can significantly impair patients' appearance, causing restricted speech and difficulty in eating, bringing substantial psychological and physiological burden to the patients.[3] Among the maxillofacial bones, the mandible is prone to various cysts and tumors,[4] superficially located and vulnerable to traumatic injury,[5] and possesses a singular blood supply making it susceptible to osteonecrosis[6] and osteomyelitis.[7] Therefore, the repair and functional reconstruction of mandibular defects has long been a focus in the field of oral and maxillofacial surgery as well as plastic surgery,[8] bearing high clinical value and scientific significance.

Mandibular defects can be categorized into small bone defects that can self-heal and critical-sized bone defects (CSBD) that cannot fully regenerate naturally. CSBD is clinically defined as defects exceeding 50% of the bone circumference or greater than 2 cm. These defects are required surgical intervention using bone graft methods.[9] Currently, bone graft materials are mainly derived from autogenous, allogeneic, and xenogeneic tissue sources.[10] Autografts are the "gold standard" source for bone grafting,[11] but their clinical application is limited due to restrictions on bone harvesting, "secondary surgery" trauma, and high incidence of complications at the donor site (8.5%–20%[12]). Allograft and xenografts pose risks such as surgical complexity, high cost, and risk of pathogenic microbial infection.[13] Bone tissue engineering uses artificially synthesized, biologically active biomaterials to achieve good bone conduction, bone generation, and osteogenesis.[14] It is considered a potential treatment method to address the clinical limitations of existing treatment approaches.

Currently, calcium phosphate (CAP) ceramics, such as hydroxyapatite (HA) and β-tricalcium phosphate (β-TCP), are commonly used as bone graft substitutes in the clinic. They share a similar crystalline structure with natural cancellous bone,[15] both exhibiting good bone induction and osteogenic activity.[16] Moreover, these materials can completely biodegrade in the body, with their degradation products Ca^{2+} and PO_4^{3-} being the main components of the bone matrix, which promote bone mineralization.[17] HA requires several years to fully degrade in the body,[18] a slow degradation rate that is not synchronized with the body's bone regeneration speed. In contrast, β-TCP can fully degrade in a matter of months,[19] facilitating the dynamic balance of scaffold degradation and tissue regeneration,[20] thus making it become a more suitable material as bone tissue engineering scaffold. Bone tissue can be divided into two types: cortical bone (also known as dense bone) and trabecular bone (also known as cancellous bone or

spongy bone). The difference between these two types of bone tissues is largely based on porosity: with the cortical bone possessing a porosity of 5% to 15%, while the porosity of trabecular bone is between 40% and 95%.[21] On the basis of scaffold materials simulating natural bone, the morphology of the bone scaffold should also adopt a structure similar to human trabecular bone. Trabecular bone is an internally interconnected three-dimensional porous structure, with pore diameters ranging from 100 to 900 μm, and the average curvature of the trabecular surface is zero.[22] Current bone scaffolds often use a log-pile structure, but their flat surfaces and sharp edges, compared to the curved and smooth cellular partitions in the body, are not conducive to cell recruitment, adhesion, and growth.[23] It has been reported that triply periodic minimal surfaces (TPMS) with periodic changes along the *X*, *Y*, and *Z* axes in Euclidean space and it has a zero average curvature,[24] which recapitulates the natural structure of cancellous bone.[25] TPMS can be divided into Gyroid (G), Diamond (D), and Schwarz P (P) surfaces.[26] Among them, the G surface, due to its relatively larger specific surface area and porosity, facilitates cellular recruitment and promotes cell adhesion,[27] in addition to exhibiting characteristics that enhance osteogenic differentiation in the body.[28]

In this present study, we investigated the use of TPMS-G surface scaffolds, adjusting the function period to control pore size, combining internal offset, external offset, and triangles to precisely control scaffold wall thickness and porosity. We determined the influence of augmenting these parameters on important scaffold characteristics such as elastic modulus, compressive strength, and permeability parameters, in addition to evaluating its regenerative capacity in vitro and in vivo within a mandibular defect model in rabbits.

Materials and methods

Design and preparation of scaffold

Using Matlab R2020a software, four G-surface scaffolds with porosities of 40%, 50%, 60%, and 70% were designed. The scaffolds were designed to be theoretically cylindrical, with a diameter of 8 mm, a height of 4 mm, and a wall thickness of 0.25 mm. The scaffolds were created as cylinders with a bottom diameter of 8 mm, a thickness of 4 mm, and a wall thickness of 200 μm. β-tricalcium phosphate (β-TCP) scaffold was prepared by additive manufacturing technology based on digital laser processing. The bone scaffold we prepared contains 85% of light cured monomers β- Triple cycle minimum curved porous ceramic scaffold with tricalcium phosphate and 15% hydroxyapatite. The process parameters for 3D printing (AUTOCERA-M, Beijing Shiwei Technology Co. Ltd, China) are as follows: the wavelength of light 405 nm, spot size 50 μm, exposure time 6 s, exposure power 30 mW/cm², and layer thickness 25 μm. After the scaffold was cleaned with single distilled water, it was sterilized within an autoclave for 30 min at 121°C and

then dried at 37°C for 12 h. We measured the long axis of the elliptic hole on the side of the support as the pore diameter (40% 0.33 mm; 50% 0.45 mm; 60% 0.60 mm; and 70% 0.87 mm).

Microscopic observation and mechanical properties test of the scaffold

Digital photos of the TPMS scaffold were taken from two perspectives using a Nikon digital camera: front and top views. A scanning electron microscope (JSM-IT500, JEOL, Japan) was used to observe the surface morphology of the scaffold. Using a universal material testing machine (INSTRON 3365, INSTRON, USA), the β-TCP scaffold was tested by axial compression to rupture, and the testing speed was 1 mm/min. Three samples were tested in each group to obtain the average value of their mechanical strength.

In vitro degradation testing

The scaffolds were divided into four groups based on porosity, with three replicate samples in each group. The scaffolds were immersed in Tris-HCl buffer (0.05 M; pH~7.4) at 37°C. At predetermined time intervals, they were retrieved, rinsed with distilled water, and dried. Changes in mass was monitored throughout the degradation period.

Cell proliferation detection

BMSCs (CP-M131, Pricella, China) were seeded on TPMS scaffolds with different porosities in 48-well plates at a density of 1×10^5/well, and cultured in a cell incubator (37°C, volume fraction of 5% CO_2). Three time points were established (1, 2, and 3 days). At each time point, 50 μL of CCK-8 solution was added to each sample and incubated in a cell incubator for 3 h. The CCK-8 solution in 48-well plate was transferred to a 96-well plate, and the absorbance value of each well was detected using the enzyme-labeled instrument (IMark, BIO-RAD, USA) at the wavelength of 450 nm. Each group of samples was repeated three times.

Cell adhesion detection

After the cells and scaffolds were cultured for 24 h, the cells were subjected to live-dead staining. A 1 mL of Calcein–AM/PI mixed staining solution was added to each well and incubated in the dark at 37°C and 5% CO_2 for 30 min. After washing with PBS, the samples were visualized under the inverted fluorescence microscope. The average total fluorescence intensity of the single well of each group of scaffolds was calculated using ImageJ software. BMSCs were cultured with the scaffold for 24 h, then the culture medium was aspirated from the well plate, moistened with PBS three times, and 1 mL of mixed staining solution of DAPI/F-actin was added to each well, and incubated in a cell incubator (37°C, volume

fraction of 5% CO_2) for 30 min in the dark. After PBS washing, the scaffold was moved to an inverted fluorescence microscope for observation. The samples were then transferred to a laser confocal dish, and three images were captured for each group on the same plane by a laser confocal microscope (TCS SP8, Leica, Germany), with magnifications of ×50, ×400, and ×1000, respectively. Then, the average value of the total fluorescence intensity of a single hole in each group was calculated by ImageJ software.

Preparation of critical mandibular bone defect model of rabbits

All animal surgical operations were carried out according to the scheme approved by the Living Animal Teaching and Research Committee of Guangdong Medical University, with the license number GDY2204012. Fifteen 6-month-old healthy male New Zealand white rabbits weighing 3 ± 0.5 kg were selected. They were randomly divided into four groups: 40% porosity, 50% porosity, 60% porosity, and 70% porosity ($n=3$ in each group). After anesthesia, the skin of the right submandibular region was prepared routinely, sterilized, and laid with sterile sheets, and a 2–3 cm incision was made parallel to the lower edge of the rabbit's mandible from the posterior direction. The epidermis and subcutaneous tissues were incised layer by layer, and muscles were bluntly separated to expose the bone surface. A circular bone drill with a diameter of 8 mm was used to create a defect in the middle of the mandibular body, and cold physiological saline was used to reduce the temperature, to make a cylindrical bone defect with a diameter of 8 mm and a depth of 4 mm. Scaffold materials with different porosity were implanted into the defect according to predetermined groups, and the muscle membrane, fascia, and skin were stitched in layers. After the operation, the 30,000 unit penicillin was injected intramuscularly 3 days, and iodophor was used to disinfect the wound to prevent postoperative infection.

Micro-CT analysis

2 months post operation, the rabbits were euthanized via anesthesia. Mandibular samples containing implanted scaffolds were collected and scanned by micro-CT. Rabbit mandibular samples were fixed in 10% neutral formalin buffer for 24 h, and then scanned by X-ray micro-CT (Xradia Versa610, ZEISS, Germany). Working conditions: voltage 70 kV, current 114 μA, scan resolution 17.5 μm, and rotation angle of 0°. The 3D projection image was reconstructed from a stack of 2D images by using CTvox software (Skyscan, Bruker Corporation, Germany).

Histological analysis

The tissues containing implants were collected and fixed with paraformaldehyde. After embedding in paraffin, the

samples were sliced by microtomes (RM2235, Leica, Germany) with a thickness of 4 μm. Then, sections were stained with Hematoxylin-Eosin (H&E) and Masson solutions to observe the tissue structure, and to evaluate the effects of scaffolds with different porosity on bone growth. Stained samples were imaged by using the biological microscope (Leica, DM500, Germany)

Immunohistochemical analysis

The sections were dewaxed to water, and the antigen retrieval was conduction using the high-pressure steam method. The expression levels of alkaline phosphatase (ALP) and osteoprotegerin (OPG) in bone tissues were detected by SABC immunohistochemical method. Stained samples were imaged using the biological microscope (Leica, DM500, Germany)

Differentially expressed genes (DEGs) analysis

Genes differential expression analysis was performed by DESeq2 software between two different groups (and by edgeR between two samples). The genes with the parameter of false discovery rate (FDR) <0.05 and absolute fold change ⩾2 were considered differentially expressed genes. Differentially expressed genes were then subjected to enrichment analysis of GO functions and KEGG pathways.

Principal component analysis

Principal component analysis (PCA) was performed with princomp function of R (http://www.r-project.org/) in this experience. PCA is a statistical procedure that converts hundreds of thousands of correlated variables (gene expression) into a set of values of linearly uncorrelated variables called principal components. PCA is largely used to reveal the structure/relationship of the samples/datas.

GO enrichment analysis

Gene Ontology (GO) is an international standardized gene functional classification system which offers a dynamic-updated controlled vocabulary and a strictly defined concept to comprehensively describe properties of genes and their products in any organism. GO has three ontologies: molecular function, cellular component, and biological process. The basic unit of GO is GO-term. Each GO-term belongs to a type of ontology.

GO enrichment analysis provides all GO terms that significantly enriched in DEGs comparing to the genome background. First, all Differentially Expressed Genes (DEGs) were aligned with Gene Ontology (GO) terms available in the Gene Ontology database (http://www.geneontology.org/). Subsequently, the gene counts for each term were computed, and significantly enriched GO terms among the DEGs were determined using the hypergeometric test, comparing them against the genome background.

Pathway enrichment analysis (KEGG)

Genes usually interact with each other to play roles in certain biological functions. Pathway-based analysis helps to further understand genes biological functions. KEGG is the major public pathway-related database. Pathway enrichment analysis identified significantly enriched metabolic pathways or signal transduction pathways in DEGs comparing with the whole genome background.

Gene set enrichment analysis (GSEA)

We performed gene set enrichment analysis using software GSEA (v4.1.0) and MSigDB to identify whether a set of genes in specific GO terms, KEGG pathways, DO terms (for Homo sapiens), Reactome (for a few model animals) shows significant differences in two groups. Briefly, we input gene expression matrix and rank genes by Signal2Noise normalization method. Enrichment scores and p value was calculated in default parameters. GO terms, KEGG pathways (DO terms, Reactome) meeting this condition with $|NES| > 1$, NOM $p < 0.05$, FDR $q < 0.25$ were considered to be different in two groups.

Alternative splicing analysis

rMATS (version 4.1.1; http://rnaseq-mats.sourceforge.net) was used to identify alternative splicing events and analyze differential alternative splicing events between samples. We identified AS events with a false discovery rate (FDR) <0.05 in a comparison as significant AS events.

Real-time quantitative polymerase chain reaction (RT-qPCR)

After co-culturing rabbit bone marrow mesenchymal stem cells with TPMS scaffolds for 14 days, the culture medium was aspirated from the wells of the plate. The wells were washed three times with 1×PBS solution, followed by the addition of 1 mL Trizol solution to each well. The scaffolds were repeatedly pipetted to extract total RNA from the cells on the scaffold. The extracted RNA was subjected to cDNA synthesis using the PrimeScript Reverse Transcription kit. Subsequently, RT-qPCR experiments were conducted using SYBR Green PCR mix (TaKaRa) and the LightCycler 480 II system (Roche, USA). The reaction conditions were as follows: initial denaturation at 95°C for 5 s; PCR quantification analysis at 95°C for 15 s, followed by 40 cycles of 60°C for 1 min; dissolution curve analysis at 95°C for 15 s, 60°C for 1 min, and 95°C for 1 min; and cooling at 50°C for 30 s. The relative expression levels of VEGFA (Vascular Endothelial Growth Factor A), S100A4 (S100 Calcium Binding Protein A4), YAP1 (Yes1 Associated Transcriptional Regulator), CSF1R (Colony Stimulating Factor 1 Receptor), and HES1 (Hes Family BHLH Transcription Factor 1) were determined by reverse transcribing 1 μg of total RNA into cDNA,

and their relative expression levels were analyzed using the $2^{-\triangle\triangle Ct}$ method for quantification analysis.

Statistical methods

The quantitative data is expressed as the mean ± standard deviation (SD). Use one-way ANOVA or Student-*t* test to compare the data. $*p < 0.05$, $**p < 0.01$, $***p < 0.001$, and $****p < 0.0001$. $p < 0.05$ is considered to be statistically significant.

Results and discussion

Morphology and mechanical properties of TPMS scaffolds

The TPMS structure was adopted to mimic the unique structure of cancellous bone with the aims to develop a biomimetic bone graft substitute. Figure 1(a) shows a macroscopic image of the TPMS bone scaffolds with a porosity of 40%, 50%, 60%, and 70%. From the images, it can be observed that the different porosity scaffolds mimic different sizes of bone trabeculae. The surface morphology and internal structure of TPMS scaffolds with different porosity were observed via scanning electron microscopy. It was found that the 3D-printed scaffolds with three-period minimal curved surfaces exhibited a curved porous structure with uniform pore size distribution (Figure 1(b)). The structure of the scaffold has continuous interlayer transitions with interconnected pore network. The surface of the scaffold is compact, and the ceramic particles are clearly visible. Research has shown that the mechanical properties of bone scaffolds are affected by the pore structure, with a clear correlation between the scaffolds porosity and mechanical properties.[29,30] Cancellous bone blocks were used as homogeneous materials in compression experiments, and various biomechanical properties were obtained as a reference. O'Mahony et al obtained the elastic modulus of cancellous bone from the edentulous mandible in three directions: the highest elastic modulus was in the proximal and distal directions, with an average of 907 ± 849 MPa; the second was in the buccal and lingual directions, with an average of 511 ± 565 MPa; and in the upper and lower directions, with an average of 114 ± 78 MPa.[31] van Eijden's study showed that the compressive strength of the mandible was between 1 and 20 MPa.[32] The compressive strength and elastic modulus of the scaffolds with different porosity were measured by universal mechanical testing machine. The results showed that the compressive strength of the scaffolds with 40%, 50%, 60%, and 70% porosity were 3.19, 3.70, 3.93, and 4.13 MPa, respectively (Fig.ure 1(c)), with the 60% ($p < 0.05$) and 70% ($p < 0.01$) groups exhibiting a significantly enhanced compressive strength when compared to the 40% group. The compressive strength values obtained were similar to that of the mandible in the buccal-lingual direction, and scaffold with high porosity usually have more pores and channels, which helps to disperse stress and prevent crack growth. This structure can increase the strength of the material. The elastic modulus of the scaffolds with 40%, 50%, 60%, and 70% porosity were 367.94, 481.42, 475.45, and 523.62 MPa respectively (Figure 1(d)), with the 50% ($p < 0.05$), 60% ($p < 0.05$), and 70% ($p < 0.01$) groups exhibiting a significantly increased elastic modulus compared to the 40% group. The compressive strength values obtained for these different scaffold designs were in a similar range as the mandible. The biodegradation test reveals that degradation rates remain similar across various porosities, but 70% group (8.84%) showed higher mass loss after 6 months, with other scaffolds ranging from 5.49%~7.16%. The bone scaffold we prepared contains 85% of the photocurable monomer β-tricalcium phosphate and 15% HA. β-TCP has good degradation properties, but the crystal structure of hydroxyapatite is stable, and the degradation rate is relatively slow.[33] The degradation rate is also affected by its large volume and compressive strength. At present, low replacement rate bone scaffolds have received attention from researchers and clinical doctors.[34] The experimental results showed that the compressive strength and elastic modulus of the scaffold were similar to the cancellous bone, and the structure, elasticity and strength of the scaffold were in accordance with the physiological characteristics of cancellous bone, which is beneficial to supporting the biomechanical functions of bone tissue.

In vitro biocompatibility analysis

In addition to the biomechanical properties of bone graft substitutes, the TPMS scaffolds should also be biocompatibility,[35,36] promote cell adhesion and proliferation to facilitate effective tissue healing. The adhesion and proliferation of BMSCs on different structures were studied. To validate the biocompatibility of 3D-printed TPMS scaffolds, BMSCs were seeded onto the scaffolds for CCK-8 cell proliferation experiments. The results showed that 70% porous scaffolds exhibited the highest rate of proliferation at three time points, followed by the 60%, 50%, and 40% scaffolds (Figure 2(b)). This profile may be due to the larger pore size of the macroporous scaffolds, which are more favorable to cell substance exchange.[37] On the other hand, low porosity scaffolds are not conducive to the internal growth of cells, resulting in a smaller area of cell growth than the scaffold with a larger pore size. Cell-seeded scaffolds from each group were then stained using live-dead staining to explore long-term cell growth. Fluorescent microscopy in conjunction with fluorescence intensity analysis (Figure 2(a) and (c)), showed that 70% porosity had the highest cell proliferation rate, followed by 60%, 50%, and 40% groups, indicating that scaffolds with greater porosity had improved cell proliferation effects than scaffolds with lower porosity.[38] The result from the CCK-8 assay and live/dead staining clearly indicate that the 70% porosity scaffold facilitated cellular proliferation to a greater degree when compared to the other scaffold groups. Laser confocal microscopy was employed to further investigate the influence of different scaffold architectures on cellular morphology within the
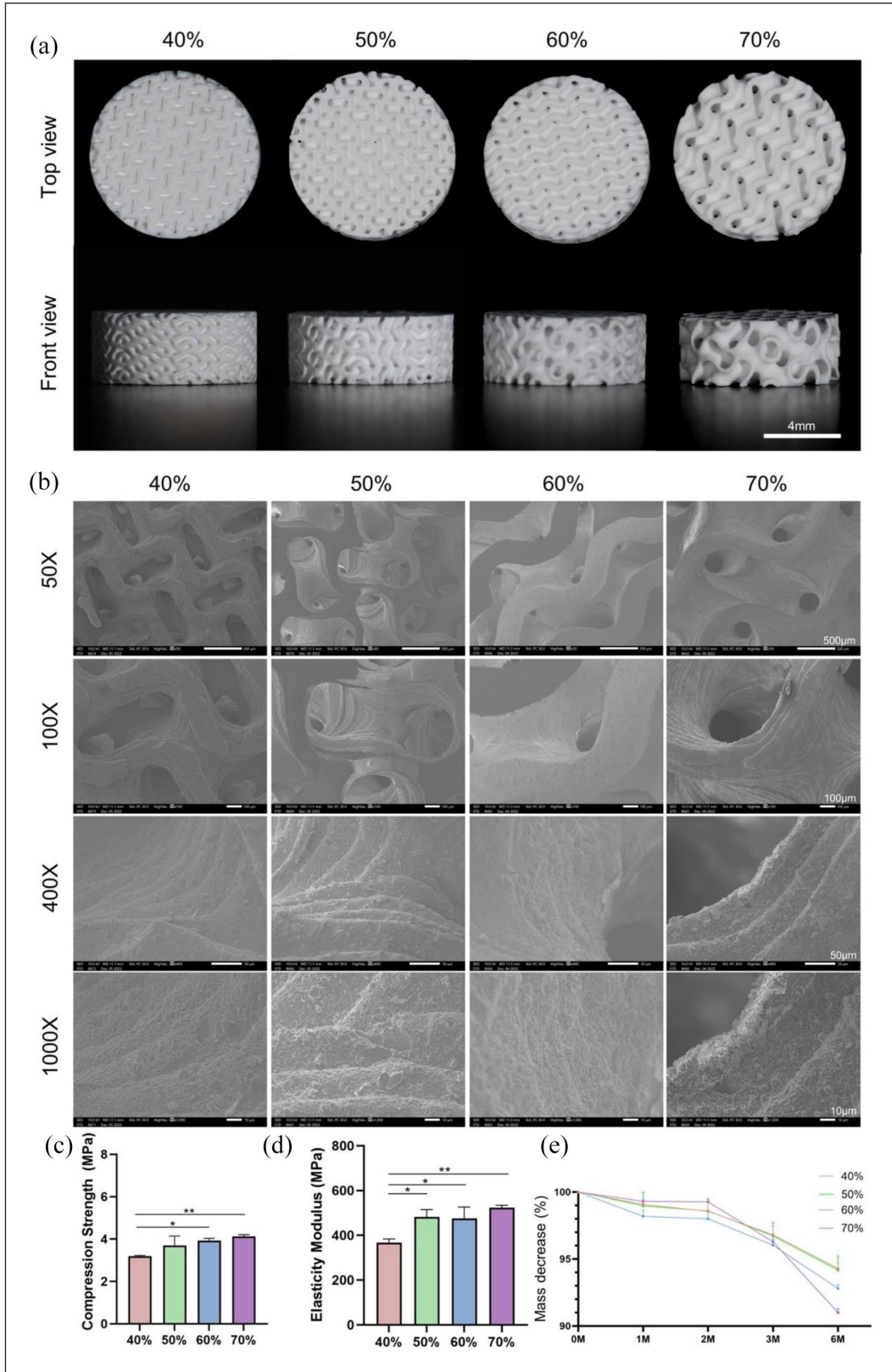
Figure 1. (a) Digital photos of TPMS bone scaffold with porosities of 40%, 50%, 60%, and 70%, (b) observing the micro-morphology of scaffolds with different porosities under scanning electron microscope, (c) the compressive strength of the scaffolds with different porosities, (d) the elastic modulus of the scaffolds with different porosities, and (e) the biodegradability of scaffolds with different porosities.
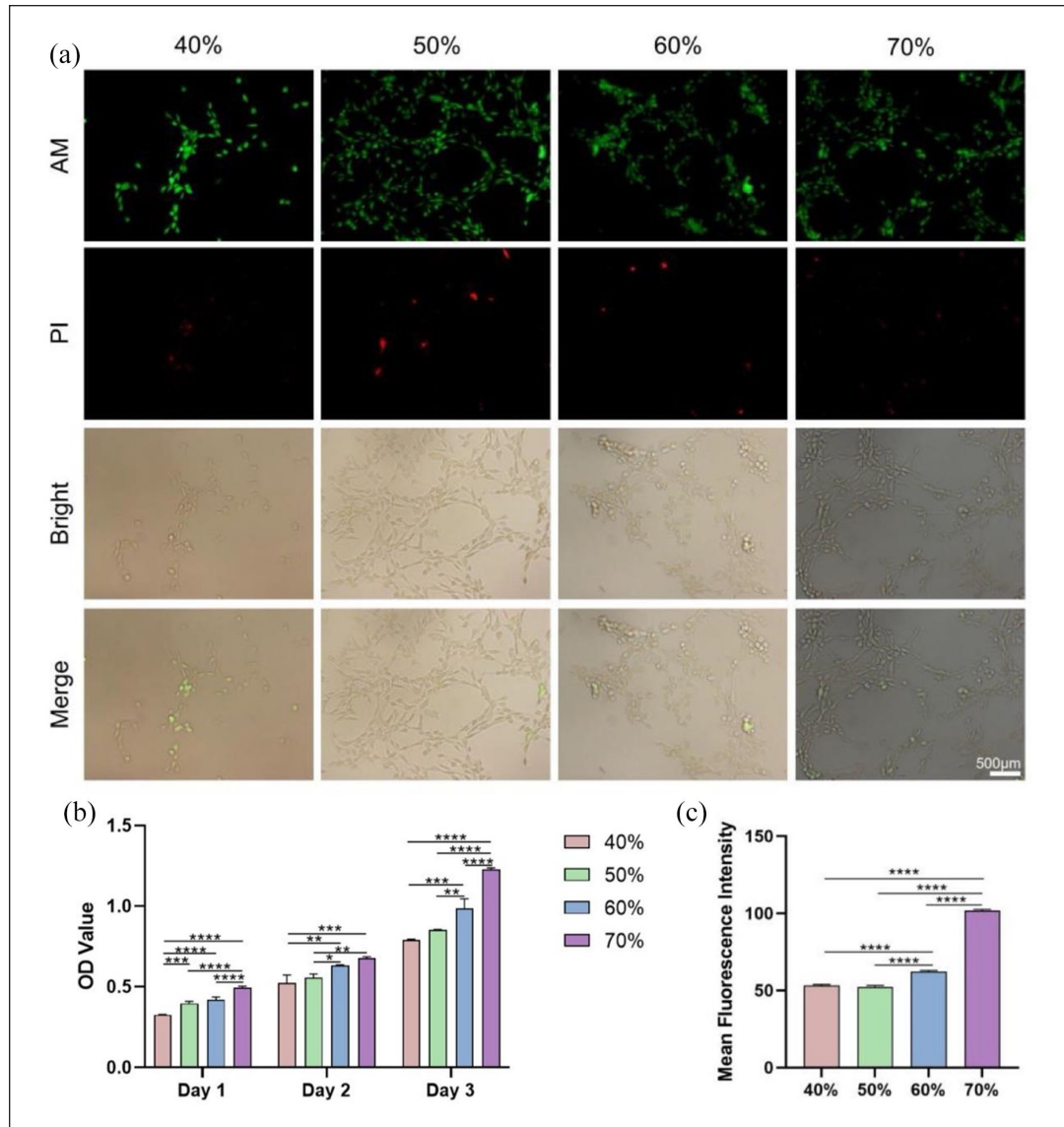
$*p < 0.05.$ $**p < 0.01.$

Figure 2. (a) Live-Dead staining of TPMS bone scaffold with 40%, 50%, 60%, and 70% porosities, (b) column analysis diagram of CCK-8 experiment, and (c) histogram of average fluorescence intensity.
*$p < 0.05$. **$p < 0.01$. ****$p < 0.0001$.

construct (Figure 3(a)). The cells within the 70% scaffolds exhibited the typical fibroblast-like morphology in addition to possessing the highest density of cells when compared to the other groups. Together, these findings indicate that the TPMS scaffolds were suitable for the early adhesion and proliferation of osteoblasts in the scaffolds of each group[39] It has been proved that, compared with the wooden crib structure, the TPMS scaffolds have greater specific surface area and surface continuity, greatly facilitating cell adhesion and growth, and thus higher cell activity during culture.[40] In addition, in order to better observe the growth and morphology of the cells on the scaffolds, and to verify that the porous TPMS scaffolds have good biocompatibility,[41,42] the cells on each group of scaffolds examined under the scanning electron microscope. As shown in Figure 3(b), the

cells in each group displayed the typical long fusiform morphology, highlighted by the blue arrow. Moreover, the images showed that the DLP-based 3D printing technology used in this study resulted in the scaffolds presenting a rough surface at the microscopic level, which is likely conducive to the attachment of osteoblasts' pseudopodia.

TPMS scaffolds facilitate the repair of mandibular defects in New Zealand white rabbits

To explore the regenerative effects of the TPMS scaffolds on mandibular repair, we established a defect model in the mandible of New Zealand white rabbits. An overview of the surgical procedure performed is shown in Figure 4(a).
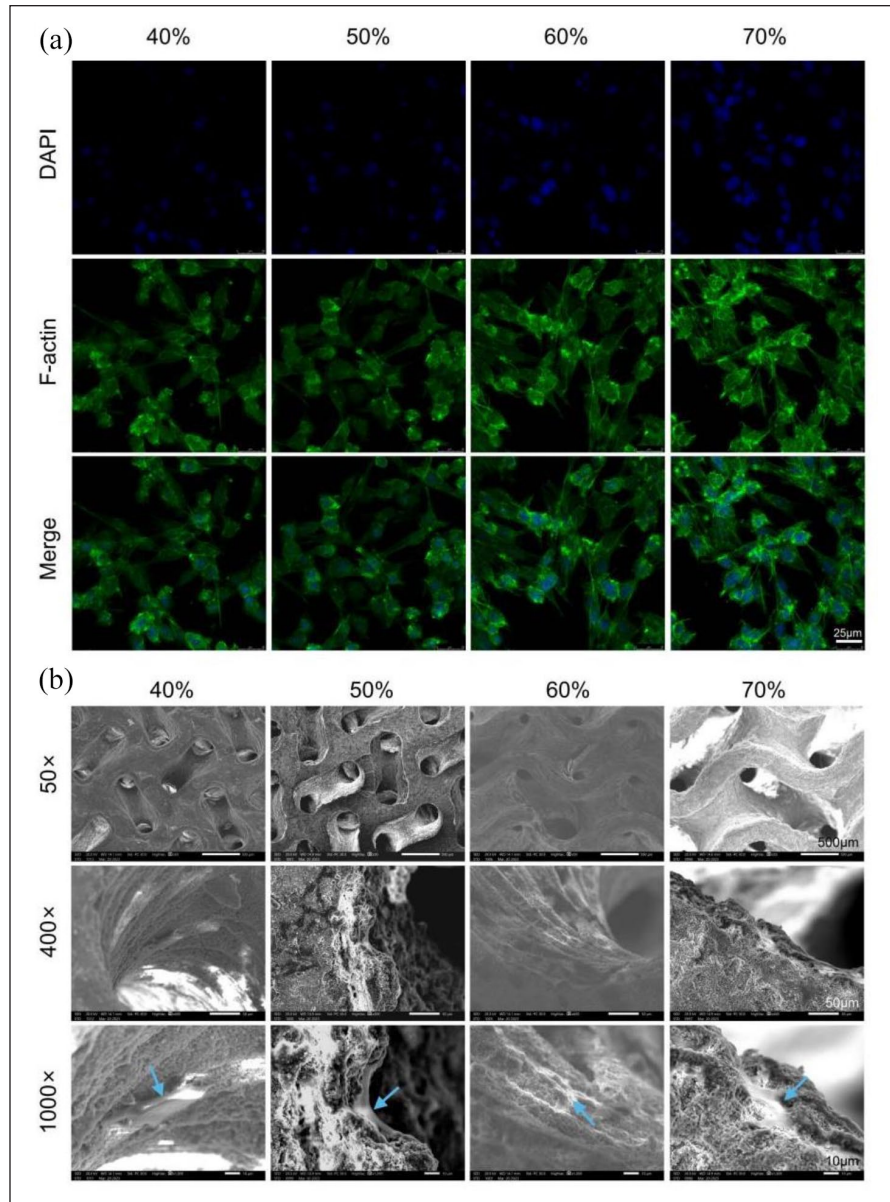
Figure 3. (a) Laser confocal images of TPMS bone scaffolds with porosity of 40%, 50%, 60%, and 70% under a 40-fold microscope (DAPI shows the nucleus, F-actin is stained with Phalloidin) and (b) scanning electron microscope images of TPMS bone scaffold with porosity of 40%, 50%, 60%, and 70%.
Blue arrows refer to mouse bone marrow mesenchymal stem cells.

The experimental animals recovered well after the operation, with no post-operative complications. Two months after surgery, the mandibles were extracted and analyzed by Micro-CT scanning. From Figure 4(b), it can be seen that the de novo low-density cancellous bone tissue in the 70% porosity scaffold has a clearer trabecular structure when compared to the scaffold designs exhibiting lower porosities. When compared to the 70% scaffold, the 40% group exhibited reduced de novo bone formation particularly in the center of the constructs. This is likely due to the low porosity scaffolds restricting nutrient transport, neovascularization, and cellular ingrowth, critical processes in effective tissue healing. Moreover, smaller pores favor

hypoxic conditions and induced osteochondral formation before osteogenesis, while large pores, that are well-vascularized, lead to direct osteogenesis.[43] The enhanced bone formation observed within the 70% scaffolds is consistent with the research that bone scaffolds with high porosity and parts close to the host bone tissue are more conducive to bone repair.[44] Micro-CT analysis of ROI area bone tissue volume (BV; Figure 4(c)), the total volume of the ROI area (TV; Figure 4(d)), the ratio of bone tissue to tissue volume can reflect changes in bone mass (BV/TV; Figure 4(e)), and the average thickness of bone trabeculae (Tb. Th) was conducted on samples (Figure 4(f)). The experimental results clearly show that the average thickness of
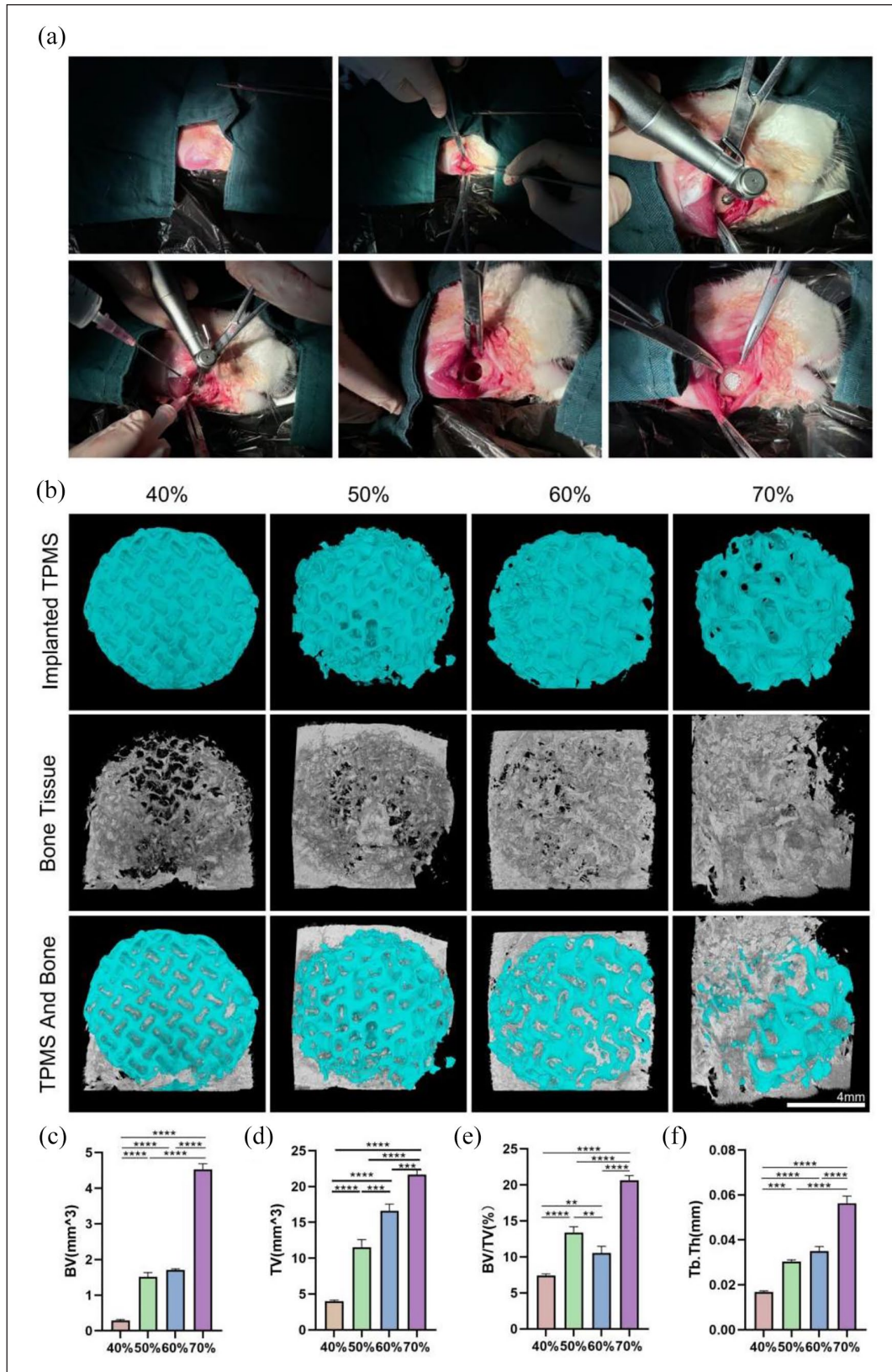
Figure 4. (a) Flow chart of mandibular defect modeling and TPMS-loaded bone scaffold in New Zealand white rabbits, (b) Micro-CT images of TPMS bone scaffolds with porosities of 40%, 50%, 60%, and 70%, (c) BV: ROI area bone tissue volume, (d) TV: The total volume of the ROI area, and (e) BV/TV: The ratio of bone tissue to tissue volume can reflect changes in bone mass. (f) Tb.Th: Average thickness of bone trabeculae.
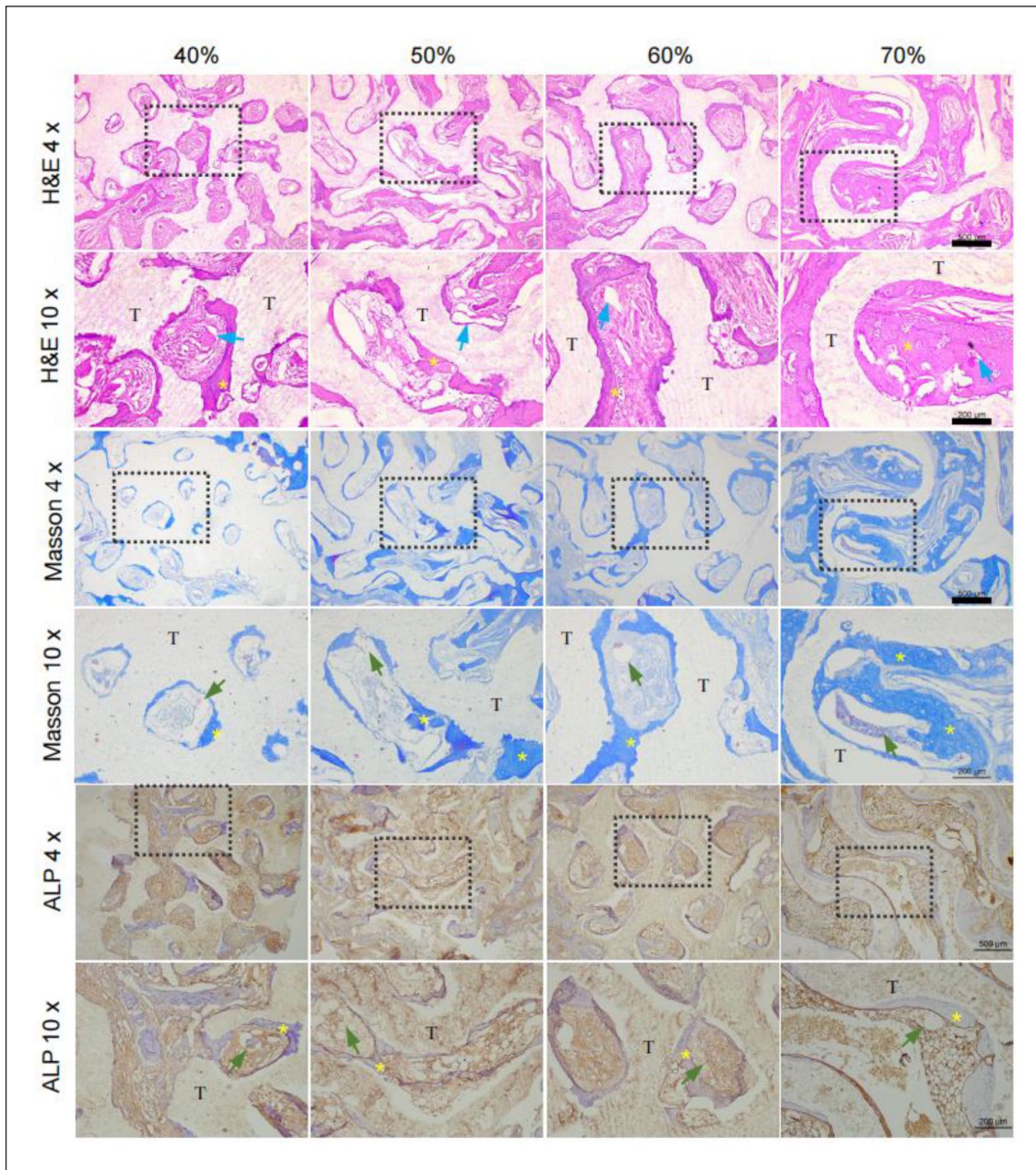$**p < 0.01.$ $***p < 0.001.$ $****p < 0.0001.$

Figure 5. Histological and immunohistochemical analysis of bone regeneration induced by TPMS scaffolds. Note: The yellow asterisks indicate mature bone tissue, the red arrows indicate new blood vessels, "T" indicates scaffolds.

newly formed bone tissue and trabeculae in the 70% porosity scaffold group was significantly higher than that of other groups (Figure 4(c)–(f); $p < 0.0001$). In addition to micro-CT analysis, the mandibles implanted with the TPMS bone scaffolds were extracted and assessed via histological (H&E and Masson trichrome staining) and immunohistochemical analysis (ALP and OPG). Several studies have highlighted the importance of scaffold porosity in facilitating bone ingrowth, allowing more cells to invade and providing a larger surface area, which is believed to contribute to higher bone-induced protein adsorption.[45,46] Our findings showed that the groups containing the 70% porosity scaffold displayed the best growth of cancellous bone (Figure 5). Immunohistochemical analysis showed that all four scaffolds groups exhibited positive staining for ALP, an early marker of bone formation, with the 70% scaffold groups displaying more concentrated ALP positive areas in the newly formed bone tissue around the scaffold. Moreover, the average fluorescence intensity of OPG was most pronounced in the groups containing the 70% scaffold when compared to the other test groups (Figure 6). In addition to osteogenic induction,
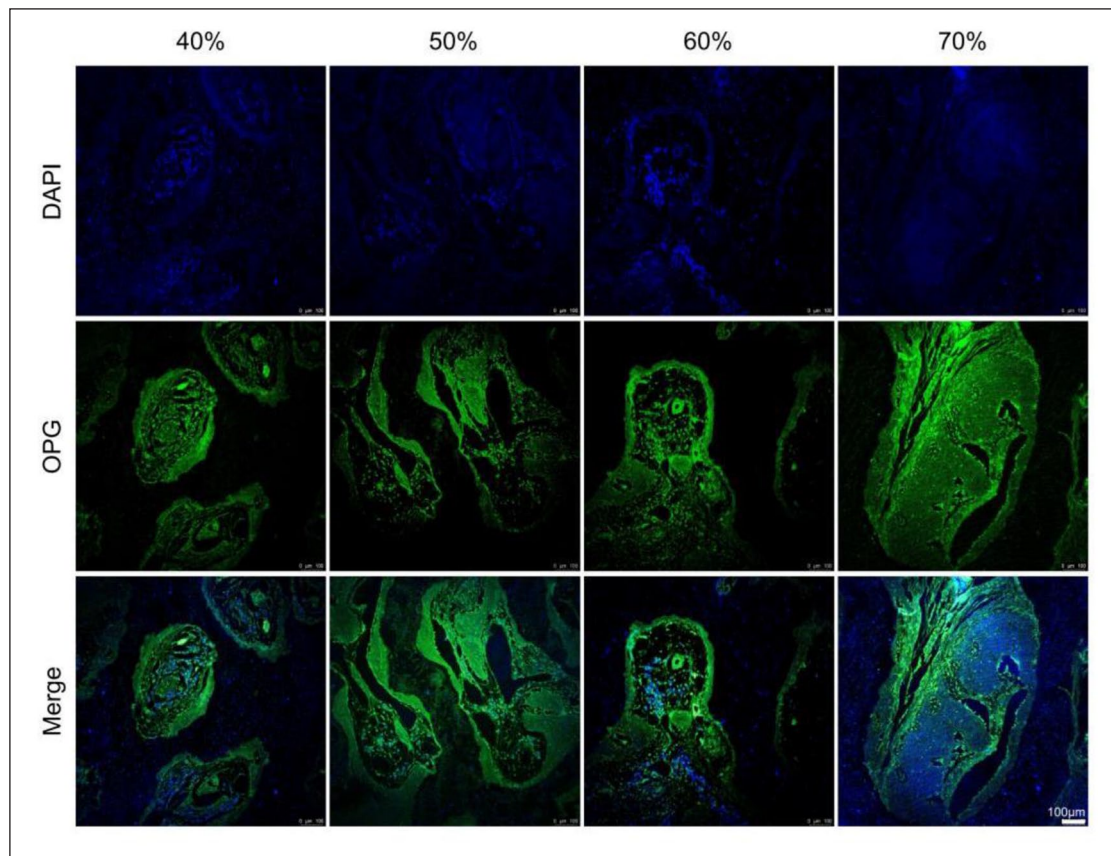
Figure 6. OPG immunofluorescent staining of bone regeneration induced by TPMS scaffolds. Note: DAPI staining blue represents the nucleus, green represents the OPG protein.

angiogenesis is a critical process involved in the effective healing of bone defects.[47] The structure and composition of bone substitutes must allow vascularization by presenting interconnected porosity and favorable biochemical support. The latter can accelerate bone remodeling by strengthening capillaries to promote the colonization and retention of osteoblasts and nutrients.[48] For bone substitutes to develop angiogenesis, pores seem to be essential in their structures. On the one hand, pore size directly plays a role in bone ingrowth,[49] ensuring cell colonization, migration, and transportation. Our findings showed that the 70% group displayed increased quantity of blood vessels (red arrow) within the constructs when compared to the other scaffold groups (Figure 5). Collectively, these findings indicate the implantation of the TPMS scaffolds promoted effective bone regeneration at the mandibular defect site, with the 70% porosity bone scaffold exhibiting the best tissue healing. In future experiments, we expect to further optimize the scaffold material with a 70% porosity. Through modification and loading of biomaterials with bioactive factors, it is expected to promote the growth of new bone and vascular tissues in the early stage. Taken together, the results in this study demonstrate the considerable potential additively manufactured TPMS scaffolds

provide as a bone graft substitute for mandibular defect repair.

TPMS scaffolds foster bone repair via activation of the Hippo pathway

To explore the mechanism of how 70% porosity bone scaffold influences BMSCs behaviors, RNA sequence analysis of mesenchymal stem cells cultured in these scaffolds for 2 weeks was analyzed. Principal components analysis of the data revealed that the 70% TPMS scaffold group samples had more similar gene expression profiles with each other than with the control samples (Figure 7(a)).

A number of genes expression was up-regulated in 70% group. Concretely, the osteoblast differentiation-related genes (e.g. REST, BMPR1A, and SMAD3) and angiogenesis-related factors (e.g. VEGFA, HES1, PDGFC, and PDGFB) were significantly upregulated in the 70% group, indicating improved bone formation ability of BMSCs (Figure 7(b)). Moreover, the gene expression of the Hippo signaling regulation pathways factors (e.g. YAP1, TCF7L2, and CSF1R) was significantly upregulated in the 70% group compared to control group (Figure 7(c)). Hippo signaling pathway is important for the regulation of tissue
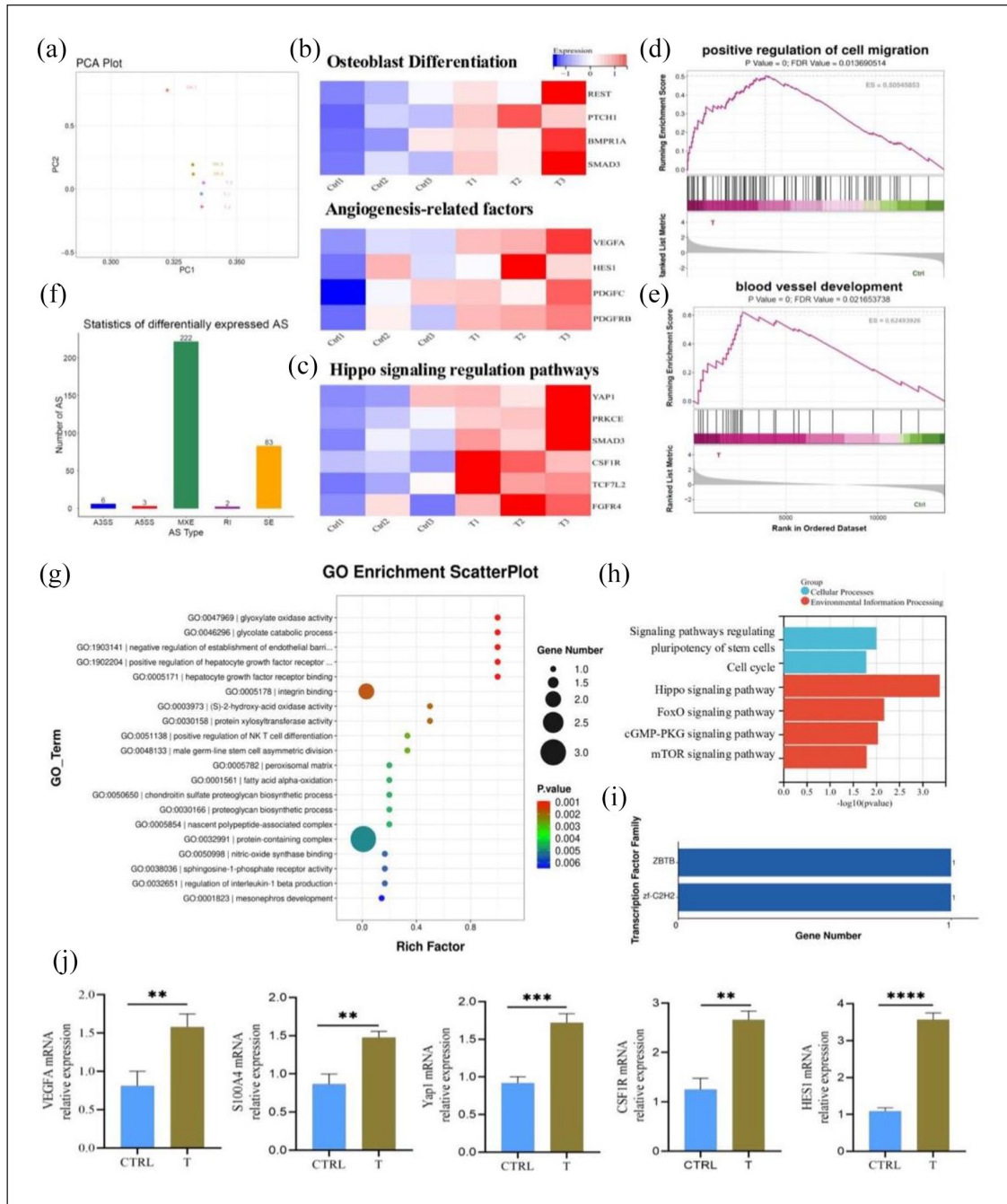
Figure 7. (a) Principal components (PC) analysis on tissues from TPMS scaffolds and tissues from control group, (b and c) Heatmaps of osteoblast differentiation-related genes, Angiogenesis-related factors and Hippo signaling regulation pathways genes expression after implant the scaffold for 2 weeks (red: high expression; blue: low expression), (d and e) GSEA enrichment analysis, (f) differential alternative splicing events between TPMS and control samples, (g) GO enrichment analysis. (h) KEGG pathway analysis of DEGs, (i) differentially expressed transcription factors family, and (j) RT-qPCR analysis of five genes (VEGFA, S100A4, YAP1, CSF1R, and HES1) related osteoblast differentiation, angiogenesis and Hippo signaling regulation pathways.

growth, tissue homeostasis and regenerative repair.[50–52] The elevated gene expression of YAP1, PRKCE, SMAD3, and CSF1R indicated an increased propensity of differentiation into osteoblast cells within the 70% group.[53,54] The RT-qPCR analysis of VEGFA, S100A4, YAP1, CSF1R, and HES1 also confirmed the higher expression of angiogenesis-related factors and Hippo signaling pathway-related genes in the 70% groups (Figure 7(j)). GSEA analysis found that the 70% group could promote the regulation of cell migration and blood vessel development

(Figure 7(d) and (e)). These results together revealed the important role of scaffold on BMSCs behaviors and bone damage repair.

Figure 7(f) shows the differentially expressed statistics of alternative splicing which mainly containing mutually exclusive exon (MXE) and skipped exon (SE). Gene ontology (GO) analysis showed that 70% TPMS scaffold induced the up-regulation of genes associated with integrin binding and positive regulation of NK T cell differentiation when compared with the control samples (Figure 7(g)). Kyoto Encyclopedia of Genes and Genomes (KEGG) analysis also revealed gene enrichment in Hippo signaling pathway (Figure 7(h)). Differential expression of transcription factors is mainly concentrated in ZBTB and zf-C2H2 family (Figure 7(i)). These results emphasized that different cytoskeletal recombination and mechanical stress transduction of BMSCs in scaffolds with different pore morphology.

Conclusion

In conclusion, this study developed a series of additively manufactured bioceramic scaffolds based on hydroxyapatite, mimicking the trabecular structure of cancellous bone for the regeneration of mandibular defects in New Zealand white rabbits. The experimental results showed that all four scaffolds displayed biocompatibility and good osteogenic capacity. In particular, the scaffolds exhibiting a 70% porosity showed significantly enhanced Hippo signaling pathway and mechanical properties, promoting osteogenic differentiation, and angiogenic in vitro and in vivo.

Author contributions

J.Z, H.Z, and J.W conceived the study; H.Z and J.W performed the experiments; Z.L and Y.Y collected and J.H analyzed the data; H.Z and M.C wrote the manuscript; J.Z. and Q.L secured the funding for the research; X.L and K.M revised the manuscript. S.W responsible for TPMS bone scaffold design. All authors approved the final version of the manuscript.

Availability of data and materials

All data needed to evaluate the conclusions in the paper are present in the paper and/or the Supplementary Materials. Additional data related to this paper may be requested from the authors.

Declaration of conflicting interests

The author(s) declared no potential conflicts of interest with respect to the research, authorship, and/or publication of this article.

Funding

Ethical approval

All animal surgical protocol was approved by the Institutional Animal Care and Use Committee at Guangdong Medical University (GDY2204012).

ORCID iD

Hong Zhu 🔟 https://orcid.org/0000-0002-2528-0753

References

1. Ferguson BM, Entezari A, Fang J, et al. Optimal placement of fixation system for scaffold-based mandibular reconstruction. *J o Mech Behav Biomed Mater* 2022; 126: 104855.
2. Paré A, Bossard A, Laure B, et al. Reconstruction of segmental mandibular defects: current procedures and perspectives. *Laryngoscope Investig Otolaryngol* 2019; 4(6): 587–596.
3. Guo J, Yao H, Li X, et al. Advanced hydrogel systems for mandibular reconstruction. *Bioactive materials* 2023, 21, 175-193.
4. Bertin H, Peries S, Amiaud J, et al. Characterization of the tumor microenvironment in jaw osteosarcomas, towards prognostic markers and new therapeutic targets. *Cancers* 2023; 15(4): 1004.
5. Brown JS, Khan A, Wareing S, et al. A new classification of mandibular fractures. *Int J Oral Maxillofac Surg* 2022; 51(1): 78–90.
6. Forner LE, Dieleman FJ, Shaw RJ, et al. Hyperbaric oxygen treatment of mandibular osteoradionecrosis: combined data from the two randomized clinical trials DAHANCA-21 and NWHHT2009-1. *Radiother Oncol* 2022; 166: 137–144.
7. Muraoka H, Ito K, Hirahara N, et al. Magnetic resonance imaging texture analysis in the quantitative evaluation of acute osteomyelitis of the mandibular bone. *Dentomaxillofac Radiol* 2022; 51(1): 20210321.
8. Nie R, Sun Y, Lv H, et al. 3D printing of MXene composite hydrogel scaffolds for photothermal antibacterial activity and bone regeneration in infected bone defect models. *Nanoscale* 2022; 14(22): 8112–8129.
9. Liu T, Fang W, Wu G, et al. Low dose BMP2-doped calcium phosphate graft promotes bone defect healing in a large animal model. *Front Cell Dev Biol* 2020; 8: 613891.
10. Amini Z and Lari R. A systematic review of decellularized allograft and xenograft-derived scaffolds in bone tissue regeneration. *Tissue Cell* 2021; 69: 101494.
11. Cohen DJ, Scott KM, Kulkarni AN, et al. Acellular mineralized allogenic block bone graft does not remodel during the 10 weeks following concurrent implant placement in a rabbit femoral model. *Clin Oral Implants Res* 2020; 31(1): 37–48.
12. Campana V, Milano G, Pagano E, et al. Bone substitutes in orthopaedic surgery: from basic science to clinical

practice. Journal of materials science. *Mater Med* 2014; 25(10): 2445–261.

13. Roddy E, DeBaun MR, Daoud-Gray A, et al. Treatment of critical-sized bone defects: clinical and tissue engineering perspectives. *Eur J Orthop Surg Traumatol* 2018; 28(3): 351–362.

14. Rauner G and Kuperwasser C. Microenvironmental control of cell fate decisions in mammary gland development and cancer. *Dev Cell* 2021; 56(13): 1875–1883.

15. Zhou H, Yang L, Gbureck U, et al. Monetite, an important calcium phosphate compound-Its synthesis, properties and applications in orthopedics. *Acta Biomater* 2021; 127: 41–55.

16. Yuan B, Wang Z, Zhao Y, et al. In vitro and in vivo study of a novel nanoscale demineralized bone matrix coated PCL/β-TCP scaffold for bone regeneration. *Macromolec Biosci* 2021; 21(3): e2000336.

17. Chang HY, Tuan WH and Lai PL. Biphasic ceramic bone graft with biphasic degradation rates. *Mater Sci Eng C Mater Biol Appl* 2021; 118: 111421.

18. Shi J, Dai W, Gupta A, et al. Frontiers of hydroxyapatite composites in bionic bone tissue engineering. *Materials* 2022; 15(23): 8475.

19. Shen C, Wang MM, Witek L, et al. Transforming the degradation rate of β-tricalcium phosphate bone replacement using 3-dimensional printing. *Ann Plast Surg* 2021; 87(6): e153–e162.

20. Stastny P, Sedlacek R, Suchy T, et al. Structure degradation and strength changes of sintered calcium phosphate bone scaffolds with different phase structures during simulated biodegradation in vitro. *Mater Sci Eng C Mater Biol Appl* 2019; 100: 544–553.

21. Karageorgiou V and Kaplan DJB. Porosity of 3D biomaterial scaffolds and osteogenesis. *Biomaterials* 2005; 26(27): 5474–5491.

22. Ha M, Athirasala A, Tahayeri A, et al. Micropatterned hydrogels and cell alignment enhance the odontogenic potential of stem cells from apical papilla in-vitro. *Dent Mater* 2020; 36(1): 88–96.

23. Jing JD. *Precise control of pore size of calcium phosphate bioactive ceramic scaffolds and effect of bone regeneration and repair*. Doctor, South China University of Technology, 2019.

24. Kelly CN, Francovich J, Julmi S, et al. Fatigue behavior of As-built selective laser melted titanium scaffolds with sheet-based gyroid microarchitecture for bone tissue engineering. *Acta Biomater* 2019; 94: 610–626.

25. He L, Liu X and Rudd C. Additive-manufactured gyroid scaffolds of magnesium oxide, phosphate glass fiber and polylactic acid composite for bone tissue engineering. *Polymers* 2021; 13(2): 270.

26. Ataee A, Li Y and Wen C. A comparative study on the nanoindentation behavior, wear resistance and in vitro biocompatibility of SLM manufactured CP-Ti and EBM manufactured Ti64 gyroid scaffolds. *Acta Biomater* 2019; 97: 587–596.

27. Shen M, Li Y, Lu F, et al. Bioceramic scaffolds with triply periodic minimal surface architectures guide early-stage bone regeneration. *Bioact Mater* 2023; 25: 374–386.

28. Wang C, Lai J, Li K, et al. Cryogenic 3D printing of dual-delivery scaffolds for improved bone regeneration with enhanced vascularization. *Bioact Mater* 2021; 6(1): 137–145.

29. Kadkhodapour J, Montazerian H and Raeisi S. Investigating internal architecture effect in plastic deformation and failure for TPMS-based scaffolds using simulation methods and experimental procedure. *Mater Sci Eng C Mater Biol Appl* 2014; 43: 587–597.

30. Man K, Joukhdar H, Manz XD, et al. Bone tissue engineering using 3D silk scaffolds and human dental pulp stromal cells epigenetic reprogrammed with the selective histone deacetylase inhibitor MI192. *Cell Tissue Res* 2022; 388(3): 565–581.

31. O'Mahony AM, Williams JL, Katz JO, et al. Anisotropic elastic properties of cancellous bone from a human edentulous mandible. *Clin Oral Implants Res* 2000; 11(5): 415–421.

32. van Eijden TM. Biomechanics of the mandible. *Crit Rev Oral Biol Med* 2000; 11(1): 123–136.

33. Zhang Q, Wang W, Schmelzer E, et al. The degradation behavior of calcium-rich hydroxyapatite foams in vitro. *J Biomed Mater Res A* 2021; 109(6): 859–868.

34. Isaacson N, Lopez-Ambrosio K, Chubb L, et al. Compressive properties and failure behavior of photocast hydroxyapatite gyroid scaffolds vary with porosity. *J Biomater Appl* 2022; 37(1): 55–76.

35. Qi J, Yu T, Hu B, et al. Current biomaterial-based bone tissue engineering and translational medicine. *Int J Mol Sci* 2021; 22(19): 10233.

36. Chen ZY, Gao S, Zhang YW, et al. Antibacterial biomaterials in bone tissue engineering. *J Mater Chem B* 2021; 9(11): 2594–2612.

37. Aarvold A, Smith JO, Tayton ER, et al. The effect of porosity of a biphasic ceramic scaffold on human skeletal stem cell growth and differentiation in vivo. *J Biom Mater Res Part A* 2013; 101(12): 3431–3437.

38. Ma T, Li Y, Yang ST, et al. Effects of pore size in 3-D fibrous matrix on human trophoblast tissue development. *Biotechnol Bioeng* 2000; 70(6): 606–618.

39. Mandal S, Viraj, Nandi SK, et al. Effects of multiscale porosity and pore interconnectivity on in vitro and in vivo degradation and biocompatibility of Fe-Mn-Cu scaffolds. *J Mater Chem B* 2021; 9(21): 4340–4354.

40. Zhang Q, Ma L, Ji X, et al. High-strength hydroxyapatite scaffolds with minimal surface macrostructures for load-bearing bone regeneration. *Adv Funct Mater* 2022; 32(33): 2204182.

41. Rajagopalan S, Robb RA. Schwarz meets Schwann: design and fabrication of biomorphic tissue engineering scaffolds. *Med Image Comput Comput Assist Interv*. 2005;8 (Pt 1):794–801.

42. Li X, Ding J, Wang J, et al. Biomimetic biphasic scaffolds for osteochondral defect repair. *Regen Biomater* 2015; 2(3): 221–228.

43. Dimitriou R, Jones E, McGonagle D, et al. Bone regeneration: current concepts and future directions. *BMC Med* 2011; 9: 66.

44. Ma S, Tang Q, Zhu C, Wang F, et al. Laser powder bed fusion-built Ti6Al4V bone scaffolds composed of sheet and strut-based porous structures: morphology, mechanical properties, and biocompatibility. *Chin J Mech Eng* 2022; 1(4): 100051.

45. Chai F, Raoul G, Wiss A, et al. Bone substitutes: Classification and concerns. *Rev Stomatol Chir Maxillofac* 2011; 112(4): 212–221.

46. Daculsi G. Biphasic calcium phosphate concept applied to artificial bone, implant coating and injectable bone substitute. *Biomaterials* 1998; 19(16): 1473–1478.

47. Fernandez de Grado G, Keller L, Idoux-Gillet Y, et al. Bone substitutes: a review of their characteristics, clinical use, and perspectives for large bone defects management. *Journal of Tissue Engineering*. 2018;9. doi:10.1177/2041731418776819

48. Geiger F, Beverungen M, Lorenz H, et al. Bone substitute effect on vascularization and bone remodeling after application of phVEGF165 transfected BMSC. *J Funct Biomater* 2012; 3(2): 313–326.

49. Malhotra A and Habibovic P. Calcium phosphates and angiogenesis: implications and advances for bone regeneration. *Trends Biotechnol* 2016; 34(12): 983–992.

50. Dey A, Varelas X and Guan KL. Targeting the Hippo pathway in cancer, fibrosis, wound healing and regenerative medicine. *Nat Rev Drug Discov* 2020; 19(7): 480–494.

51. Zhang N, Bai H, David KK, et al. The Merlin/NF2 tumor suppressor functions through the YAP oncoprotein to regulate tissue homeostasis in mammals. *Dev Cell* 2010; 19(1): 27–38.

52. Koontz LM, Liu-Chittenden Y, Yin F, et al. The Hippo effector Yorkie controls normal tissue growth by antagonizing scalloped-mediated default repression. *Dev Cell* 2013; 25(4): 388–401.

53. Komatsu N, Kajiya M, Motoike S, et al. Type I collagen deposition via osteoinduction ameliorates YAP/TAZ activity in 3D floating culture clumps of mesenchymal stem cell/extracellular matrix complexes. *Stem Cell Res Ther* 2018; 9(1): 342.

54. Lorthongpanich C, Thumanu K, Tangkiettrakul K, et al. YAP as a key regulator of adipo-osteogenic differentiation in human MSCs. *Stem Cell Res Ther* 2019; 10(1): 402.